CHEMISTRY OF MATERIALS
Cite This: Chem. Mater. 2019, 31, 7752–7760
Article
pubs.acs.org/cm

Dopant Selection Strategy for High-Quality Factor Localized Surface Plasmon Resonance from Doped Metal Oxide Nanocrystals

Bharat Tandon,[†,‡] Sandeep Ghosh,[†] and Delia J. Milliron*[,†]

[†]McKetta Department of Chemical Engineering, The University of Texas at Austin, Austin, Texas 78712-1589, United States
[‡]Department of Chemistry, Indian Institute of Science Education and Research, Dr. Homi Bhabha Road, Pune 411008, India

Supporting Information

ABSTRACT: Thin films of degenerately doped metal oxides such as those of Sn-doped In_2O_3 ($Sn:In_2O_3$) are commercially significant for their broad utilization as transparent conducting electrodes in optoelectronic devices. Over the past decade, nanocrystals (NCs) of $Sn:In_2O_3$ and other doped metal oxides have also attracted interest for localized surface plasmon resonance (LSPR) that occurs in the near- to mid-infrared region. The suitability of this LSPR for some applications depends on its capacity to concentrate light in small regions of space, known as near-field hot spots. This efficiency to create near-field hot spots can be judged through an LSPR figure-of-merit such as Quality factor (Q-factor), defined as the ratio of LSPR peak energy to its line width. The free electron density determines the LSPR peak energy, while the extent of electron scattering controls the LSPR line width; hence, these factors together essentially dictate the value of the Q-factor. An unfortunate trade-off arises when dopants are introduced since the aliovalent dopants generating the free electrons (increasing LSPR energy) also act as centers of scattering of electrons (increasing LSPR line width), thereby decreasing the LSPR Q-factor. Dopant selection is hence of paramount importance to achieve a high value of LSPR Q-factor. Here, we describe the properties of aliovalent cationic dopants that allow both high LSPR energy and low LSPR line width and, subsequently, high LSPR Q-factor. In this context, we identify Zr^{4+} as a model aliovalent dopant for high LSPR Q-factor in the In_2O_3 lattice. The resulting Zr-doped In_2O_3 NCs exhibit one of the highest LSPR Q-factors reported in the mid-infrared region while also performing equivalently to the recognized materials for either high dopant activation ($Sn:In_2O_3$ NCs) or low LSPR line width (Ce-doped In_2O_3 NCs) simultaneously. The Zr donor level is positioned well inside the conduction band of In_2O_3, and Zr doping is surface segregated, both minimizing electron scattering. The combination of this low electron scattering and high dopant activation of Zr^{4+} ions is responsible for the high LSPR Q-factors. These strategies can be used to design a variety of doped metal oxide NC systems exhibiting high LSPR Q-factors.

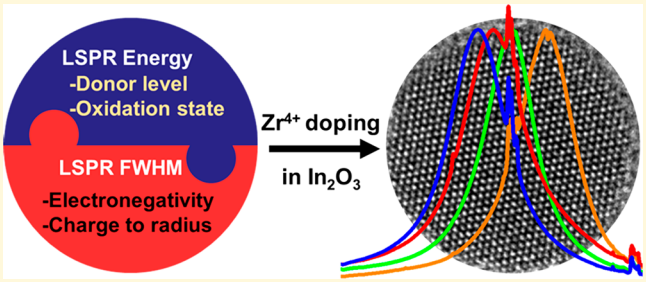

Thin films of degenerately doped metal oxides have been long utilized as transparent conducting electrodes in solar cells and photovoltaics due to their unusual ability to combine the properties of visible light transparency and high electrical conductivity in one material.[1] Owing to the same free electron properties, nanocrystals (NCs) of such degenerately doped metal oxides also exhibit mid- to near-infrared localized surface plasmon resonance (LSPR).[2−7] The LSPR response is induced by the generation of free charge carriers (electrons in case of n-doped metal oxides discussed here), which collectively oscillate at resonant frequencies. These LSPR active NCs may find applications in sensing,[8−10] photothermal therapy,[11] photovoltaics,[12] electrochromic coatings,[13−15] and advanced spectroscopies such as surface-enhanced infrared absorption (SEIRA).[3] For many of these potential applications, the potential of these NCs to create intense localized electric fields (hot spots) around them is essential. In general, LSPR excitations can effectively focus electric fields into volumes well below the diffraction limit, but this is not yet well established for doped metal oxide materials. The potential efficiency of hot spot generation can be assessed indirectly by a figure of merit derived from the LSPR response known as the Quality factor (or Q-factor), which is defined as the ratio of the LSPR peak energy to its full width at half-maximum (fwhm). LSPR peak energy depends on the free carrier density in the NCs, while the fwhm reflects the extent of carrier scattering, e.g., by charged point defects in the NC lattice.[16] Consequently, a high Q-factor suggests stronger near-field enhancements, longer plasmon lifetimes, and weaker electronic damping. Hence, it becomes important to consider two significant impacts of dopants in metal oxide NCs: (a) changing free electron density leading to tuning of the LSPR energy and (b) scattering the motion of oscillating free electrons leading to damping of the LSPR.

In some cases, the relatively high value of the high-frequency dielectric constant of the host material enables unusually high

Received: July 22, 2019
Revised: August 20, 2019
Published: September 9, 2019

DOI: 10.1021/acs.chemmater.9b02917
Chem. Mater. 2019, 31, 7752−7760

LSPR Q-factors through shielding the electrostatic interactions between the dopants and the electrons. This is generally the case for doped CdO,[17] such as NCs of In-doped CdO,[18] and F, In-codoped CdO.[19] Regardless of the dielectric characteristics of the host material, a high LSPR Q-factor can conceivably be engineered based on the selection of the aliovalent dopant. For instance, Sn^{4+} is a shallow donor in In_2O_3, donating electrons to the conduction band of In_2O_3 and increasing the LSPR energy.[20−22] However, apart from acting as ionized donor impurities, Sn dopants in In_2O_3 also hybridize with In 5s orbitals, leading to significant renormalization of the band curvature at the conduction band minimum,[23−25] thereby changing the effective mass, increasing the LSPR fwhm, and decreasing the electron mobility.[16] Cerium is an alternative dopant for In_2O_3 or a codopant with Sn that has been reported to minimize ionized impurity scattering. Ce^{4+} introduces defect states deep in the conduction band of In_2O_3, well away from the conduction band edge, leading to a narrow LSPR fwhm. Unfortunately, Ce^{4+} is readily reduced to Ce^{3+}, so dopant activation is low, especially at higher dopant concentrations, and the LSPR energy achievable by this strategy is limited.[26] In each case—either Sn and Ce-doped In_2O_3 NCs—one attribute of the dopant substantially limits the LSPR Q-factor, and yet these materials still exhibit among the highest Q-factor values in the near-infrared. Therefore, there is a potential to enhance LSPR Q-factor further through a combination of high LSPR energy and low LSPR fwhm. Achieving this requires identification of dopants through their fundamental properties which will simultaneously increase LSPR energy and diminish fwhm as dopants interact with the crystal lattice, ultimately leading to high LSPR Q-factors.

The LSPR frequency ω_{LSPR} can be described by eq 1

$$\omega_{LSPR} = \sqrt{\frac{\omega_p^2}{(\varepsilon_\infty + 2\varepsilon_m)} - \Gamma^2} \tag{1}$$

where ε_∞ is the high-frequency dielectric constant of the material, ε_m is the dielectric constant of the medium surrounding the NCs, and Γ is the damping constant. Since, ε_∞ is a characteristic property of the material that is not expected to change with doping and ε_m is fixed by the environment (the solvent in the case of dispersed NCs), the controllable parameters with a strong influence on the LSPR frequency are the damping constant (that determines LSPR fwhm) and the bulk plasma frequency ω_p, which is given by

$$\omega_p^2 = \frac{ne^2}{\varepsilon_0 m^*} \tag{2}$$

where n is the free carrier density, e is the electronic charge, ε_0 is the permittivity of air/vacuum, and m^* is the effective mass of the free charge carriers (electrons or holes).[27] Since e and ε_0 are constants, the LSPR energy is directly dependent on the carrier density and the effective carrier mass. In this regard, two scenarios can be envisaged when it comes to generating free charge carrier density by a cationic substitutional doping in metal oxides: (a) when the dopant level exists close to the conduction band minimum (shallow donor) and (b) when the dopant states reside well inside the conduction band of the host. As an example of the first scenario, a shallow donor (such as Sn in In_2O_3) hybridizes with the conduction band minimum triggering renormalization of conduction band curvature, and therefore, a flatter band with higher effective carrier mass is obtained.[28] This hybridization leads to a lower ω_p, and hence, a donor level inside the conduction band is preferred over a shallow donor for generation of free electrons and raising of ω_p.[26,28,29] Additionally, generation of free electrons can be hindered if the dopant exhibits multiple stable oxidation states, if electron acceptors are present,[26,30−33] or if defect clusters introduce electron trapping sites.[23,34−36] These compensation effects are highly undesirable as they decrease the dopant activation (number of electrons generated per dopant). One can estimate the feasibility of change in oxidation state through the standard reduction potentials. Metal ions exhibiting multiple oxidation states with large positive values of standard reduction potentials are not likely to perform as ideal dopants for generation of high electron density. For example, the standard reduction potential for reduction of Ce^{4+} to Ce^{3+} is +1.44 V as a result of which Ce^{4+} doping in In_2O_3 suffers from the problem of low dopant activation.[26]

The damping constant Γ is a reflection of electron scattering though mechanisms typically including electron−electron and electron-phonon scattering, which are not necessarily the dominant electron scattering mechanisms in doped metal oxide NCs. When the size of a NC becomes much smaller than the bulk mean free path of carrier in a material, surface scattering can be significant.[37] In doped metal oxides NCs, at all sizes electrostatic interactions between the dopant ions and the electrons can significantly impact scattering. This phenomenon is known as ionized impurity scattering,[16] and the LSPR fwhm can be limited by the strength of this electrostatic interaction, which can be described by the Lewis acidity of the dopant. According to the quantitative description given by Zhang et al.,[38] the Lewis acidity L of an ion is expressed as

$$L = \frac{Z}{r^2} - 7.7\chi + 8.0 \tag{3}$$

where Z is the charge on an ion, r is the radius of the ion, and χ is the electronegativity of the element. A stronger Lewis acid (large L) will, therefore, be a better aliovalent dopant than a weaker one. This is because a high charge to radius ratio polarizes the electron cloud of the oxygen more strongly, reducing its capability as a scattering center. On the other hand, a smaller electronegativity value than the host cation ensures that the interactions between the free electrons and the dopant cations are minimized. In terms of electronic band structure, this means that the dopant levels lie higher in energy than the conduction band minimum of the host lattice. Owing to this alignment, Ce, which has a low electronegativity value, leads to a much larger L value (smaller LSPR fwhm) than Sn[21,26] in In_2O_3 despite Sn exhibiting a higher charge to radius ratio.[39] However, a very large Lewis acidity can also lead to trapping of charge carriers due to electron-acceptor behavior of Lewis acids. Nonetheless, to obtain a low LSPR fwhm in In_2O_3 NCs, a dopant with a charge-to-radius ratio greater than In and an electronegativity value smaller than In is desired. However, a large change in charge to radius ratio with respect to the host cation can also produce significant lattice strain in the host lattice and may even induce formation of a secondary phase.

In consideration of the above, Zr^{4+} appears to be a compelling candidate as a dopant in In_2O_3. Zr is almost always found in the +4 oxidation state (standard reduction potential $Zr^{4+}/Zr = -1.45$ V), which makes it an aliovalent dopant in the In_2O_3 lattice (Zr_{In}) Recent calculations by Xu et al. have shown that donor levels for Zr lie deep inside the conduction band of In_2O_3 (which can be ascribed largely to its

DOI: 10.1021/acs.chemmater.9b02917
Chem. Mater. 2019, 31, 7752−7760

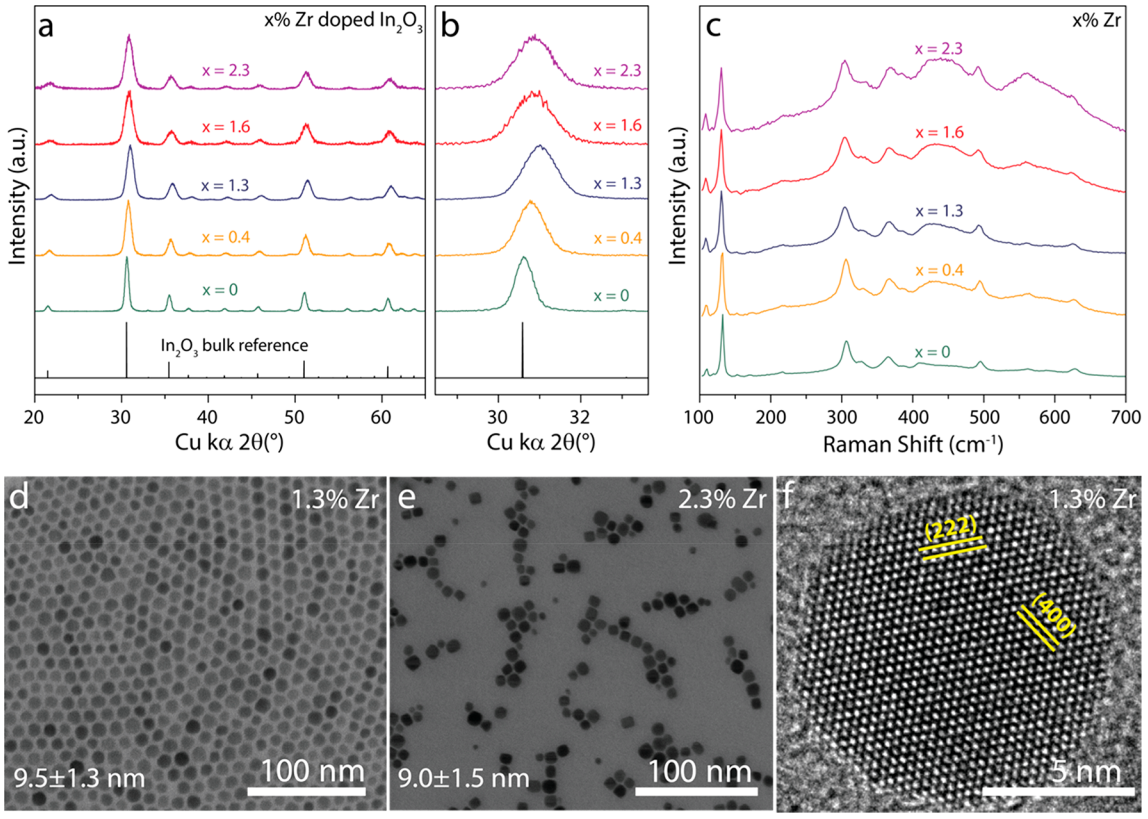

Figure 1. Characterization of Zr:In_2O_3 NCs: (a) comparison of XRD patterns with bulk In_2O_3 reference (JCPDS 88-2160) indicating retention of the cubic bixbyite structure across doping concentrations, (b) shift in the XRD peaks with incorporation of Zr^{4+} ions, (c) Raman spectroscopy signifying the absence of any impurity phase, amorphous or crystalline, (d and e) STEM images showing nearly spherical NCs with a narrow size distribution, (f) high-resolution TEM image showing the single-crystalline nature of the NCs with interplanar distances corresponding to different planes in the In_2O_3 structure.

lower electronegativity than In) and proposed it to be a prospective dopant of choice for high-mobility transparent conducting oxides.[28] The occurrence of Zr donor levels deep inside the conduction band means that the curvature of the conduction band minimum is not expected to be affected by doping and electrons donated will have a low carrier effective mass close to the $0.22m_e$ of the parent In_2O_3 material. Moreover, the ionic radius of Zr^{4+} (74 pm) matches closely with that of In^{3+} (79 pm), signifying that no significant lattice strain is anticipated from the substitution of In with Zr while sustaining a higher charge-to-radius ratio than In.[40] We, therefore, hypothesized that Zr doping in In_2O_3 NCs could lead to a high Q-factor LSPR with high dopant activation and low fwhm, which would also imply an increased mobility of electrons. Prior experimental reports showing high electron mobilities in Zr-doped In_2O_3 thin films[41−43] encouraged us to develop a synthesis for Zr-doped In_2O_3 (Zr:In_2O_3) NCs and examine their mettle as an LSPR active material.

We report here the colloidal synthesis of Zr:In_2O_3 NCs by a procedure involving alcoholysis of metal carboxylates.[44,45] In brief, using standard Schlenk line techniques operating under inert N_2 atmosphere, 8 mL of 0.5 M mixture of In and Zr precursors, indium(III) acetate and zirconium(IV) acetylacetonate, respectively, was dissolved in oleic acid at 150 °C. A mixture of these was injected at a rate of 0.2 mL/min into 13 mL of oleyl alcohol held at 290 °C. After the reaction, the solution was cooled down, and the resultant NCs were washed with ethanol and dispersed in different nonpolar solvents for further characterization. The synthesis and characterization details are described in sections S1 and S2 of the Supporting Information, respectively. The doping percentages reported herein were obtained using inductively coupled plasma optical emission spectroscopy (ICP-OES).

The structure of the NCs was assessed by X-ray diffraction (XRD, Figure 1a). At all dopant concentrations, the NCs have the same cubic bixbyite structure as the parent In_2O_3 and no impurity peaks are present. Moreover, as the Zr doping percentage is increased, the diffraction peaks first shift to higher 2θ values (signifying a decrease in the lattice constant) and then shift back to smaller 2θ values, suggesting an interplanar distance similar to undoped In_2O_3 NCs (Figure 1b). The ionic radius of Zr^{4+} is smaller than that of In^{3+},[40] which could be expected to lead to a gradual decrease in the lattice constant with an increase in Zr doping percentage, in accordance with Vegard's law.[46] The observed trend is more complex since the lattice constant increases as doping percentages above 1.5%. However, similar trends have routinely been reported in doped metal oxides and, in particular, in Sn:In_2O_3, where the lattice expansion is attributed to the repulsion between the Sn^{4+} ions which cannot be compensated entirely by the electron density in the lattice.[22,47,48] We suggest that a similar mechanism is underlying the trend reported here with Zr^{4+} ions incorporated in the In_2O_3 lattice across the range of compositions we synthesized, with competing factors influencing the lattice constant. Our understanding that Zr is well incorporated in the lattice is further substantiated by the systematic increase in the fwhm of the XRD peaks with an increase in Zr doping

DOI: 10.1021/acs.chemmater.9b02917
Chem. Mater. 2019, 31, 7752−7760

signifying a systematic decrease in the crystallite size. We note here that inhomogeneous strain in the NCs can also broaden the XRD peaks, but it is unlikely to follow a systematic trend with Zr doping. We complemented the XRD analysis with Raman spectroscopy to assess the potential formation of any amorphous or impurity phases (Figure 1c). Regardless of Zr dopant concentration, the Zr:In_2O_3 NCs exhibit the same phonon modes as undoped In_2O_3 NCs, suggesting that no significant amorphous or crystalline impurity phases are present.[31,49,50] The trend of XRD peak widths suggesting a decrease in NC size with an increase in Zr doping percentage is confirmed by direct observations using scanning transmission electron microscopy (STEM) (Figure 1d, 1e, S1, and S2). The morphology of the NCs vary between spherical to nearly cubic, which is attributed to the varied amounts of water present in the reaction vessel that leads to passivation of {001} facets by hydroxyl groups.[44] The high-resolution TEM images in Figure 1f show the single-crystalline nature of Zr:In_2O_3 NCs and interplanar distances corresponding to different lattice planes in the cubic bixbyite structure, further confirming the crystalline structure of the synthesized NCs.

To ascertain the oxidation state of the Zr ions in the In_2O_3 NCs, we employed X-ray photoelectron spectroscopy (XPS) on all of the Zr: In_2O_3 NCs and plotted the obtained spectra in the Zr 3d region (Figure 2a). Zr $3d_{5/2}$ and Zr $3d_{3/2}$ binding

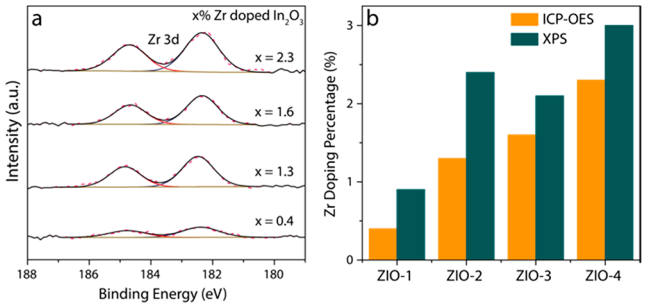

Figure 2. Dopantoxidation state and radial distribution: (a) XPS of the Zr 3d region for different Zr:In_2O_3 NCs with single-component fits (black) to the experimental spectra (pink) shown, (b) comparison of ICP-OES and XPS doping percentages revealing that Zr doping is surface segregated as doping percentages obtained for the surface (XPS) is more than the overall NC composition (ICP-OES). Notations ZIO-1 to ZIO-4 on the *x* axis just represent NCs with 4 different Zr doping percentages.

energy peaks located at 182.3 and 184.7 eV correspond to Zr in the +4 oxidation state,[51,52] progressively increasing in intensity with an increase in the Zr doping. The spectra could be fit using only one component, which further indicates the presence of Zr in a single oxidation state.

To determine the radial distribution of Zr in the NC, we compared the doping percentages obtained from XPS and ICP-OES. XPS gives an estimation of the surface doping percentage, whereas ICP-OES is a measure of overall NC composition (surface and core). Doping percentages obtained from XPS are significantly greater than those from ICP-OES (Figure 2b), suggesting that Zr is slightly surface segregated; in other words, Zr^{4+} ions preferentially substitute at In sites nearer to the surface of the NCs. Although the precise mechanism responsible for surface segregation of Zr dopants could not be elucidated, we hypothesize that using precursors with different reactivity (indium(III) acetate, a highly reactive In precursor versus the only moderately reactive Zr precursor, zirconium(IV) acetylacetonate) alters the kinetics of incorporation of In and Zr ions during NC growth and ultimately affects the radial distribution of dopants.[53] Surface-segregated doping can be favorable as previous work has shown that it is associated with narrow LSPR and high Q-factors.[21,22,54] Dopants segregated near the surface allow charge carriers to move inside the lightly doped or undoped NC core without scattering from ionized impurities. The reduced scattering significantly minimizes LSPR damping, thereby decreasing the LSPR fwhm and enhancing electron mobility.

All of the Zr:In_2O_3 NCs show remarkably narrow LSPR absorption with their LSPR energies monotonically increasing with an increase in Zr dopant concentration, signifying the donor behavior of Zr^{4+} ions (Figures 3 and S3). The LSPR of

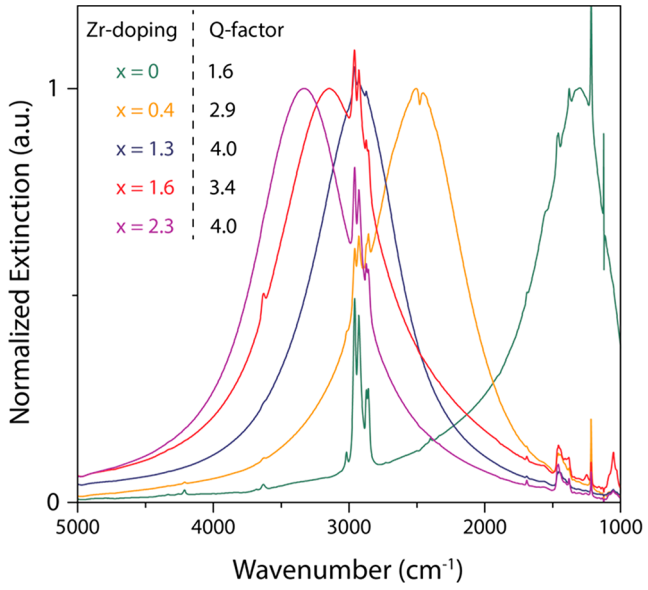

Figure 3. Optical extinction spectra of different Zr:In_2O_3 NCs displaying narrow and symmetric LSPR bands increasing in energy with an increase in Zr doping. Spectra were taken by FTIR of NCs dispersed in tetrachloroethylene.

undoped In_2O_3 NCs is attributed to the accumulation of electron density due to oxygen vacancies, whereas in Zr:In_2O_3 NCs, Zr doping is largely responsible for generating the free electrons. The highly symmetric shapes of the LSPR peaks in Figure 3 indicate there is little ionized impurity scattering,[16,21,22,27] consistent with our initial hypothesis. The LSPR parameters of different Zr:In_2O_3 NCs are listed in Table ST1. Quantitatively, the LSPR fwhm of 735 cm^{-1} (91 meV) for 1.3% Zr:In_2O_3 NCs is very close to that reported for Ce-doped In_2O_3 NCs (77 meV),[26] In-doped CdO (67 meV),[18] and smaller than the lowest reported LSPR fwhm for Sn:In_2O_3 (99 meV)[22] and other doped metal oxide NCs (Table ST2); hence, Zr:In_2O_3 NCs exhibit one of the narrowest LSPR peaks yet reported. In terms of LSPR Q-factor, Zr:In_2O_3 NCs display rather high values over a range of LSPR energies that are almost identical to those of Ce-doped In_2O_3NCs and subsequently one of the highest in the literature. Electron concentrations achievable with Ce doping are limited by the stability of the Ce^{3+} ion, which is increasingly preferentially as compared to Ce^{4+} at high doping percentages, thereby reducing the dopant activation. Consequently, the LSPR in Ce-doped In_2O_3 NCs was tunable only over a narrow range at

DOI: 10.1021/acs.chemmater.9b02917
Chem. Mater. 2019, 31, 7752−7760

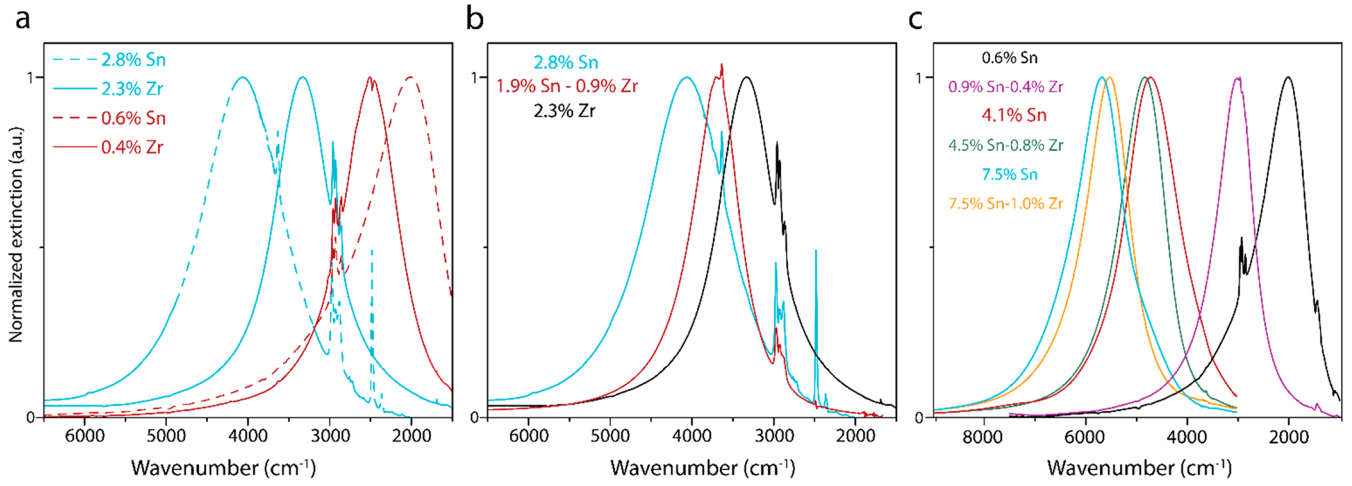

Figure 4. FTIR spectra of doped In_2O_3NCs. Establishing the high dopant activation behavior but better aliovalent nature of Zr^{4+} ions over Sn^{4+} ions by comparing FTIR spectra in (i) Series-1, Zr:In_2O_3 and Sn:In_2O_3 NCs with similar doping percentage, (ii) Series-2, Zr:In_2O_3, Sn,Zr:In_2O_3, and Sn:In_2O_3 NCs with similar total cation doping percentage, (iii) Series-3, Sn,Zr:In_2O_3 and Sn:In_2O_3 NCs with similar Sn doping percentage, all showing that for the same doping percentage, Zr:In_2O_3 and Sn,Zr:In_2O_3 NCs have similar LSPR energies but higher LSPR Q-factors as compared to Sn:In_2O_3 NCs.

low energy.[26] Therefore, Zr:In_2O_3 NCs are a more tunable option for applications where high LSPR Q-factors are desirable.

In addition to observing low LSPR fwhm and high Q-factors, we investigated dopant activation in Zr:In_2O_3 NCs, which is a measure of the extent of electron density accumulation for a given doping percentage. Dopant activation is generally high in NCs of the prototypical doped metal oxide material Sn:In_2O_3 NCs,[21,22,54] owing to shallow Sn donor levels in proximity to the conduction band minimum of In_2O_3.

To evaluate the efficacy of Zr^{4+} as an electron donor, we designed three different comparison series with Sn. Series-1 compares LSPR spectra of Zr:In_2O_3 and Sn:In_2O_3 NCs with similar doping percentages. Series-2 compares LSPR spectra at a fixed doping percentage achieved through (i) only Zr doping, (ii) only Sn doping, and (iii) Zr and Sn codoping. Series-3 measures the effect of small amounts of Zr codoping on LSPR spectra of different Sn:In_2O_3 NCs. The characterization data for these NCs (XRD and STEM images along with size distribution histograms) are given in Figures S4−S6. The optical extinction spectra obtained from these series are plotted in Figure 4, and their respective LSPR parameters are tabulated in Table ST1.

Series-1 compares optical extinction spectra of Zr:In_2O_3 NCs and Sn:In_2O_3 NCs at two different doping percentages, small (∼0.5%) and intermediate (∼2.5%) (Figure 4a). Zr:In_2O_3 NCs have a higher peak LSPR energy than Sn:In_2O_3 NCs at small doping percentage. However, at intermediate doping percentage, the Sn:In_2O_3 NCs have a higher LSPR energy than Zr:In_2O_3 NCs, potentially due to the difference in the doping level in those two samples and the smaller size of Zr:In_2O_3 NCs as compared to Sn:In_2O_3 NCs, which can decrease dopant activation.[22] Nonetheless, for both doping levels, the LSPR energies for Zr and Sn are in the same range, indicating that both of them have similar donor efficiency. The difference, however, lies in the shape and fwhm of the LSPR. For similar doping percentages, the LSPR of Zr:In_2O_3 NCs is highly symmetric compared to the asymmetric peaks of Sn:In_2O_3 NCs. Additionally, the LSPR fwhm of the Zr:In_2O_3 NCs is at least 20% narrower than that of Sn:In_2O_3 NCs (Table ST1), which is reflected in the significantly higher LSPR Q-factors of Zr:In_2O_3 NCs than Sn:In_2O_3 NCs. Unfortunately, we could not achieve higher doping concentration with Zr doping because of the low solubility limit of Zr in In_2O_3.[43] NCs are sometimes able to surpass the bulk solubility limit, but even after repeated trials using different Zr and In precursors, we were in this case not successful at increasing the doping concentration further.[55]

Series-2 compared NCs with similar overall doping percentage (∼2.5%) but different dopant composition: (i) 2.3% Zr doping, (ii) 2.8% Sn doping, or (iii) 1.9% Sn−0.9% Zr codoping in In_2O_3 NCs. The purpose was to assess how the LSPR Q-factor depends on the nature of the dopants. The LSPR energies are almost equivalent for the various dopant combinations, but the LSPR fwhm of Zr:In_2O_3 and Sn,Zr:In_2O_3 NCs is much smaller than that observed for Sn:In_2O_3 NCs (Figure 4b). In fact, as listed in Table ST1, the LSPR fwhm of 1.9% Sn−0.9% Zr-codoped In_2O_3 NCs is almost one-half of that of 2.8% Sn:In_2O_3 NCs. Consequently, there is a 50% enhancement in the LSPR Q-factor for the former compared to the latter. The Q-factor of 5.3 for 1.9% Sn−0.9% Zr-codoped In_2O_3 NCs is the highest Q-factor reported in the mid-infrared region and rivals the Q-factors of even the best-performing materials in the near-infrared LSPR literature (Table ST2). Both Series-1 and Series-2 are thus strong indicators of the advantages of Zr over Sn as a dopant in the In_2O_3 NC lattice.

To check the efficiency of Zr^{4+} in reducing electron scattering from ionized impurities, we made Series-3, where a small amount of Zr (0.5−1.0%) was codoped with small (∼1%), intermediate (∼5%), and high (∼8%) Sn doping percentages to form Sn,Zr:In_2O_3 NCs and compared these with Sn:In_2O_3 NCs having roughly the same Sn doping percentage. Since Zr^{4+} is an aliovalent donor, doping in small amounts is expected to shift the LSPR energy, but if it contributes to ionized impurity scattering, it would also induce an increased line width (fwhm) of the LSPR band.

We observe that Zr codoping in Sn:In_2O_3 NCs leads to an increase in the LSPR energy (as compared to Sn:In_2O_3 NCs with the same Sn doping percentage) for both low and

DOI: 10.1021/acs.chemmater.9b02917
Chem. Mater. 2019, 31, 7752−7760

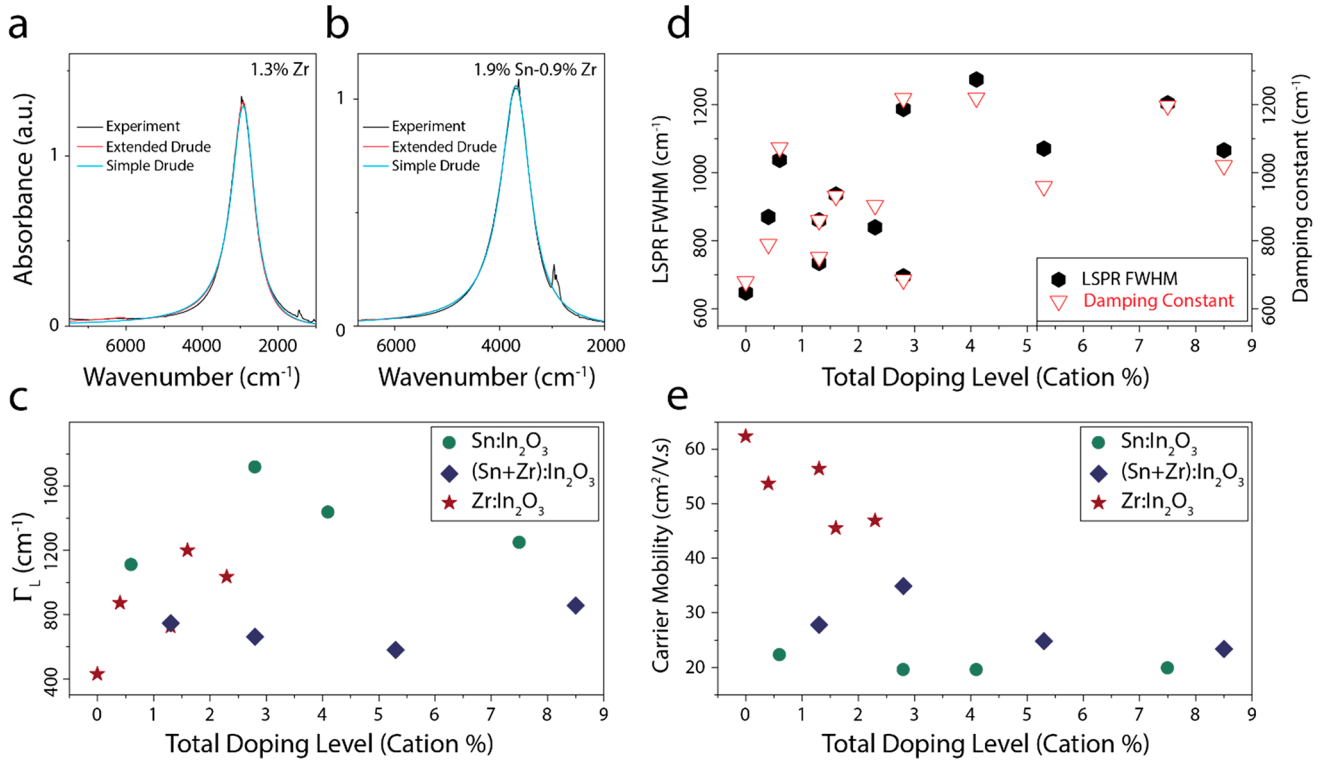

Figure 5. Fitting of the optical extinction spectra using the simple and extended Drude models. (a and b) Representative Drude model fits to the LSPR spectra of 1.3% Zr-doped and 0.9% Sn−0.4% Zr-codoped In_2O_3 NCs showing excellent fitting. (c) Comparison of the low-frequency damping constants obtained from extended Drude model fits for different NCs indicating much smaller values of Γ_L and hence low electron scattering for Zr:In_2O_3 and Sn,Zr:In_2O_3 NCs than for Sn:In_2O_3 NCs. (d) Correlation between damping constant obtained from simple Drude model fits and experimental LSPR fwhm signifying frequency independence of electron scattering in almost all NCs. (e) Comparison of optical electron mobilities obtained from the simple Drude model shows 3 times enhancement by changing the dopant from Sn^{4+} to Zr^{4+} due to reduced electron scattering.

intermediate Sn doping percentages. For high Sn doping concentration, however, codoping Zr with Sn leads to a decrease in the LSPR energy. Zr codoping in Sn:In_2O_3 leads to a decrease in the size of the NCs (increase in surface to volume ratio), which places more Sn ions close to the surface than in the core for a constant doping percentage. Since surface Sn dopants have been found to be less activated than the core Sn dopants, a decrease in NC diameter brings down the overall activation of Sn dopants, leading to smaller LSPR energies.[16,22] Zr codoping in Sn:In_2O_3 NCs also decreases the LSPR fwhm and induces a highly symmetric line shape to the LSPR band. This observation, which is constant across all Sn,Zr:In_2O_3 NCs, is also reiterated by the LSPR parameters (Table ST1), where Sn,Zr:In_2O_3 NCs are found to display LSPR fwhm approximately 20% smaller than their Sn:In_2O_3 NCs counterparts. Correspondingly, a 20% enhancement in the LSPR Q-factor is seen despite a decrease in LSPR energy for the 1.0% Zr−7.5% Sn-codoped In_2O_3 NCs. Since the degree of surface segregation of the Sn dopants is similar between Sn:In_2O_3 NCs and Sn,Zr:In_2O_3 NCs, we do not consider changes in dopant radial distribution as a potential contributor to the decrease in the LSPR fwhm (Figure S7 and S8). Therefore, Zr doping in In_2O_3 can be associated with high Q-factors, and 1.0% Zr−7.5% Sn-codoped In_2O_3 NCs exhibit an LSPR Q-factor of 5.3 (identical to 0.9% Zr−1.9% Sn), among the highest in the literature (Table ST2). Hence, the three series give conclusive evidence that Zr doping in In_2O_3 NCs leads to a combination of high dopant activation, narrow LSPR line width, and high Q-factor.

For a further quantitative interpretation we modeled the LSPR response of all of our NCs with the simple Drude and the extended Drude models by employing a MATLAB code. Since the optical properties of a material are governed by its complex dielectric function, both the carrier density and the damping of charge carriers can be accounted for by considering the free carrier contribution to the complex dielectric function.[16,27] For noble metals, this is given by the simple Drude model which can be represented as

$$\varepsilon_D = \varepsilon_\infty - \frac{\omega_p^2}{\omega^2 + i\omega\Gamma} \tag{4}$$

where ω_P is the bulk plasma frequency defined in eq 2, ε_∞ is the high-frequency dielectric constant, Γ is the damping constant, and ω is the angular frequency of the incoming electromagnetic radiation. However, this simple Drude model does not take into account the contribution of ionized impurity scattering, which is a major scattering mechanism in doped semiconductors. For this purpose, in doped semiconductor systems we often use the extended Drude model where the frequency-independent damping constant Γ in the simple Drude is replaced by a frequency-dependent analogue $\Gamma(\omega)$ symbolized through the empirical equation[16]

$$\Gamma(\omega) = \Gamma_L - \frac{\Gamma_L - \Gamma_H}{\pi}\left[\tan^{-1}\left(\frac{\omega - \Gamma_X}{\Gamma_W}\right) + \frac{\pi}{2}\right] \tag{5}$$

DOI: 10.1021/acs.chemmater.9b02917
Chem. Mater. 2019, 31, 7752−7760

where Γ_L and Γ_H are the low-frequency and high-frequency damping constants, respectively, Γ_X is the crossover-frequency from the low- to the high-frequency region, and Γ_W is the width of the crossover region. The value of Γ_L qualitatively signifies the extent of scattering by ionized dopants, and therefore, to achieve a low LSPR fwhm and symmetric LSPR band, Γ_L should be minimized. Since the extent of carrier scattering is determined by the damping constants, carrier mobilities can also be derived optically from the damping function using

$$\mu_{opt} = \frac{e}{m^*\Gamma(0)} \quad (6)$$

where we assume that the electrostatic potential at low frequencies would be equivalent to the carriers moving under the influence of a dc electric field, and therefore, we employ $\Gamma(0)$, which is the value of the damping function at zero frequency.[21]

Using the methodology described in section S3, we fitted the optical extinction spectra of all NCs with both the simple and the extended Drude models and extracted the values of the bulk plasma frequency, electron density, damping constants, and optical electron mobilities. Representative plots for both Zr:In_2O_3 and Sn,Zr:In_2O_3 NCs are shown in Figure 5a and 5b, respectively, and fitting parameters are tabulated for simple Drude and extended Drude models in Tables ST3 and ST4, respectively. The residual fits are presented in Figure S9. Excellent fits could be achieved for all of the Zr-doped NCs for both the simple Drude and the extended Drude models, suggesting that only the free electron density is responsible for the optical absorption.

Discussing the fit parameters for the extended Drude model first, almost all Zr:In_2O_3 and Sn,Zr:In_2O_3 NCs have a small Γ_L (and $\Gamma_L \ll \Gamma_H$), crossover frequency Γ_X at energies much higher than the LSPR peak position, and narrow crossover width (Γ_W). These observations are strong indications that there is minimized impurity scattering in both Zr:In_2O_3 and Sn,Zr:In_2O_3 NCs and electron scattering in these NCs is largely frequency independent. In contrast, Sn:In_2O_3 NCs with similar doping concentration are found to have $\Gamma_L \gg \Gamma_H$, small crossover frequencies, and large crossover widths. This indicates that ionized impurity scattering is still prominent in these NCs, which contributes to broadened LSPR line widths. Regardless of this, both 4.1% and 7.5% Sn:In_2O_3 NCs display appreciably high LSPR Q-factors, which can be attributed in part to the observed slight surface segregation of Sn at high doping percentages that has been found to decrease the electrostatic interactions between the electrons and the ionized dopants and also to their large size, which decreases surface scattering. However, the overall trend that Zr:In_2O_3 and Sn,Zr:In_2O_3 NCs exhibit much smaller Γ_L than Sn:In_2O_3 NCs (which leads to high LSPR Q-factors) with the same doping percentage is robust, as evident by Figure 5c. The smallest Γ_L is exhibited by undoped In_2O_3 NCs, which is understandable because electrons therein are only scattered by the oxygen vacancies unlike doped In_2O_3 NCs where aliovalent dopants act as majority scattering centers with additional contribution from oxygen vacancies. Furthermore, comparing the electron density obtained from the extended Drude (Table ST3) fittings reveals that Sn and Zr have similar electron density for the same doping percentage, which is in agreement with our initial hypothesis and the results obtained from Series 1−3. A direct consequence of the low Γ_L is reflected in the high mobility values obtained for Sn,Zr:In_2O_3 and Zr:In_2O_3 NCs (Table ST3). However, since electron scattering in our NCs seems to be operating through a frequency-independent mechanism, we will instead use parameters derived by fitting to the simple Drude model, which has fewer fit parameters and minimizes uncertainty, to draw additional conclusions about the electronic properties. Moreover, the optical spectra of some NCs have a contribution from the C−H vibrational stretch absorption of the ligands around 3000 cm^{-1}, which complicates quantitative fitting of the LSPR; this overlapping signal can lead to unreasonably large variations in the value of the parameters in some cases, which is less of a challenge if the fit is constrained with fewer free parameters.

Nonetheless, as described before, excellent fits could be achieved by modeling the absorption spectra through the simple Drude model signifying that the electron scattering mechanism in Zr:In_2O_3 and Sn,Zr:In_2O_3 NCs is largely frequency independent, similar to that of noble metal NCs. The estimated values of bulk plasma frequency and electron density (Table ST4) are roughly equivalent to those determined from the extended Drude model. From Table ST4 one can observe that the damping constants for both Zr:In_2O_3 and Sn,Zr:In_2O_3 NCs are very close to that of the undoped In_2O_3 NCs and significantly smaller than those of the Sn:In_2O_3 NCs, which reiterates our claims of minimized ionized impurity scattering in Zr:In_2O_3 and Sn,Zr:In_2O_3NCs. A perfect correlation was observed between the damping constants and the experimental LSPR fwhm for almost all of the NCs, as shown in Figure 5d. This signifies that the simple Drude model is a good representation of the LSPR, and frequency-dependent damping is not needed to describe the dominant electron scattering processes in our NCs, especially Zr:In_2O_3 and Sn,Zr:In_2O_3 NCs. Using the single damping constant in eq 6, we determined the electron mobilities of different NCs and plotted them in Figure 5e. The electron mobilities of Zr:In_2O_3 NCs are almost 3 times greater than that of Sn:In_2O_3 NCs and lie very close to that of the undoped In_2O_3 NCs. Even the Sn,Zr:In_2O_3 NCs exhibit electron mobilities 30−80% greater than Sn:In_2O_3 NCs and close to those reported for Ce-doped In_2O_3 NCs. For the electron mobility calculations the effective carrier mass for Sn:In_2O_3 and Sn,Zr:In_2O_3 NCs was approximated as $0.39m_e$, whereas that for Zr:In_2O_3 NCs was $0.22m_e$ as suggested by Xu et al.[28] Even if the same effective carrier mass is assumed, the electron mobilities in Zr:In_2O_3 NCs would be equivalent if not greater than that of Ce-doped In_2O_3 NCs.[26] We attribute this extraordinary electronic quality of Zr:In_2O_3 NCs to the optimized position of the Zr defect level in the electronic band structure of In_2O_3 coupled with surface-segregated Zr doping, which ensures that the electrostatic potentials experienced by the electrons do not change significantly through the lattice of In_2O_3 (see Figure S10 for schematic description). These effects combine to produce a rare combination of high LSPR Q-factor, high dopant activation, and low levels of electron scattering, implying high electron mobilities, all in one material.

In conclusion, we describe the salient properties of an aliovalent dopant that determines its merit in generating high LSPR Q-factor in doped metal oxide NCs. For high LSPR energy, a donor state deep in the conduction band of the host and a stable oxidation state is required, whereas a small LSPR fwhm demands a higher charge to radius ratio and lower electronegativity of the dopant cation with respect to the host

DOI: 10.1021/acs.chemmater.9b02917
Chem. Mater. 2019, 31, 7752−7760

cation. Using these selection criteria, we propose Zr^{4+} as an ideal aliovalent dopant in the In_2O_3 lattice and report the synthesis of Zr-doped In_2O_3 NCs for the first time. The resulting $Zr:In_2O_3$ NCs exhibit a rare combination of high dopant activation and low LSPR fwhm, leading to one of the highest Q-factors in the literature on plasmonic nanomaterials. We further prove that our $Zr:In_2O_3$ NCs are comparable to the best materials for dopant activation (Sn-doped In_2O_3 NCs) and LSPR fwhm (Ce-doped In_2O_3 NCs) simultaneously. Drude fittings of the optical spectra reveal that the electron mobilities in our $Zr:In_2O_3$ NCs are 3 times as that of $Sn:In_2O_3$ NCs and equivalent to undoped In_2O_3 NCs, indicating that ionized impurity scattering is essentially absent in our $Zr:In_2O_3$ NCs. We conclude that the optimized placement of Zr donor levels in the conduction band of In_2O_3 and surface-segregated doping of Zr are responsible for the enhanced electron mobilities and could very much enable $Zr:In_2O_3$ NCs and films based on these as benchmark materials for applications such as transparent conducting electrodes to be used in flat panel displays and thin film photovoltaics. Since a high Q-factor also facilitates enhanced plasmonic hot spot generation and near-field enhancement, we are confident that $Zr:In_2O_3$ NCs would be an excellent system for applications like SEIRA and plasmonic sensing. Advancements in the colloidal synthesis of $Zr:In_2O_3$ NCs will permit one to achieve higher levels of Zr incorporation in the In_2O_3 lattice and one would, therefore, be able to achieve high LSPR Q-factor through the entire near- to mid-infrared range. The approach for this rational dopant selection can ideally be applied to any other metal oxide system like TiO_2, ZnO, and SnO_2, and additional research in this direction could allow realization of advantageous properties from a broad range of host compositions. A first glimpse of the extendibility of this strategy can be seen in Figure S11, where Hf^{4+} doping in In_2O_3 (the chemical properties of Hf are very similar to Zr due to lanthanide contraction) also leads to a narrow LSPR in the mid-infrared range.

■ ASSOCIATED CONTENT

Supporting Information

The Supporting Information is available free of charge on the ACS Publications website at DOI: 10.1021/acs.chemmater.9b02917.

Details of nanocrystal characterization (STEM, XPS, XRD) and Drude modeling scheme along with the fits to the optical extinction spectra and parameters obtained (PDF)

■ AUTHOR INFORMATION

Corresponding Author

*E-mail: milliron@che.utexas.edu.

ORCID

Bharat Tandon: 0000-0003-1108-9859

Sandeep Ghosh: 0000-0002-1149-9199

Delia J. Milliron: 0000-0002-8737-451X

Notes

The authors declare no competing financial interest.

■ ACKNOWLEDGMENTS

B.T., S.G., and D.J.M. acknowledge support from the National Science Foundation (NSF, CHE-1609656), the Alfred P. Sloan Foundation (FG-2016-6446), an NSF MRSEC (DMR-1720595), the Welch Foundation (F-1848), and the Fulbright-Nehru Doctoral Research Programme. We also thank Ms. Camila Saez Cabezas of UT Austin for help with Raman measurements and Mr. Deepak Khurana of IISER-Pune for assistance with Drude modeling.

■ REFERENCES

(1) Minami, T. New n-Type Transparent Conducting Oxides. *MRS Bull.* **2000**, *25*, 38−44.

(2) Agrawal, A.; Cho, S. H.; Zandi, O.; Ghosh, S.; Johns, R. W.; Milliron, D. J. Localized Surface Plasmon Resonance in Semiconductor Nanocrystals. *Chem. Rev.* **2018**, *118*, 3121−3207.

(3) Willets, K. A.; Van Duyne, R. P. Localized Surface Plasmon Resonance Spectroscopy and Sensing. *Annu. Rev. Phys. Chem.* **2007**, *58*, 267−297.

(4) Faucheaux, J. A.; Stanton, A. L. D.; Jain, P. K. Plasmon Resonances of Semiconductor Nanocrystals: Physical Principles and New Opportunities. *J. Phys. Chem. Lett.* **2014**, *5*, 976−985.

(5) Liu, X.; Swihart, M. T. Heavily-Doped Colloidal Semiconductor and Metal Oxide Nanocrystals: An Emerging New Class of Plasmonic Nanomaterials. *Chem. Soc. Rev.* **2014**, *43*, 3908−3920.

(6) Tandon, B.; Ashok, A.; Nag, A. Colloidal Transparent Conducting Oxide Nanocrystals: A New Infrared Plasmonic Material. *Pramana* **2015**, *84*, 1087−1098.

(7) Agrawal, A.; Johns, R. W.; Milliron, D. J. Control of Localized Surface Plasmon Resonances in Metal Oxide Nanocrystals. *Annu. Rev. Mater. Res.* **2017**, *47*, 1−31.

(8) Haes, A. J.; Hall, W. P.; Chang, L.; Klein, W. L.; Van Duyne, R. P. A Localized Surface Plasmon Resonance Biosensor: First Steps toward an Assay for Alzheimer's Disease. *Nano Lett.* **2004**, *4*, 1029−1034.

(9) Sannomiya, T.; Hafner, C.; Voros, J. In situ Sensing of Single Binding Events by Localized Surface Plasmon Resonance. *Nano Lett.* **2008**, *8*, 3450−3455.

(10) Verellen, N.; Van Dorpe, P.; Huang, C.; Lodewijks, K.; Vandenbosch, G. A. E.; Lagae, L.; Moshchalkov, V. V. Plasmon Line Shaping Using Nanocrosses for High Sensitivity Localized Surface Plasmon Resonance Sensing. *Nano Lett.* **2011**, *11*, 391−397.

(11) Jain, P. K.; Huang, X.; El-Sayed, I. H.; El-Sayed, M. A. Noble Metals on the Nanoscale: Optical and Photothermal Properties and Some Applications in Imaging, Sensing, Biology, and Medicine. *Acc. Chem. Res.* **2008**, *41*, 1578−1586.

(12) Atwater, H. A.; Polman, A. Plasmonics for Improved Photovoltaic Devices. *Nat. Mater.* **2010**, *9*, 205−213.

(13) Garcia, G.; Buonsanti, R.; Llordes, A.; Runnerstrom, E. L.; Bergerud, A.; Milliron, D. J. Near-Infrared Spectrally Selective Plasmonic Electrochromic Thin Films. *Adv. Opt. Mater.* **2013**, *1*, 215−220.

(14) Garcia, G.; Buonsanti, R.; Runnerstrom, E. L.; Mendelsberg, R. J.; Llordes, A.; Anders, A.; Richardson, T. J.; Milliron, D. J. Dynamically Modulating the Surface Plasmon Resonance of Doped Semiconductor Nanocrystals. *Nano Lett.* **2011**, *11*, 4415−4420.

(15) Wang, Y.; Runnerstrom, E. L.; Milliron, D. J. Switchable Materials for Smart Windows. *Annu. Rev. Chem. Biomol. Eng.* **2016**, *7*, 283−304.

(16) Lounis, S. D.; Runnerstrom, E. L.; Llordés, A.; Milliron, D. J. Defect Chemistry and Plasmon Physics of Colloidal Metal Oxide Nanocrystals. *J. Phys. Chem. Lett.* **2014**, *5*, 1564−1574.

(17) Mendelsberg, R. J; Zhu, Y.; Anders, A. Determining the Nonparabolicity Factor of the CdO Conduction Band using Indium Doping and the Drude Theory. *J. Phys. D: Appl. Phys.* **2012**, *45*, 425302.

(18) Gordon, T. R.; Paik, T.; Klein, D. R.; Naik, G. V.; Caglayan, H.; Boltasseva, A.; Murray, C. B. Shape-Dependent Plasmonic Response and Directed Self-Assembly in a New Semiconductor Building Block, Indium-Doped Cadmium Oxide (ICO). *Nano Lett.* **2013**, *13*, 2857−2863.

DOI: 10.1021/acs.chemmater.9b02917
Chem. Mater. 2019, 31, 7752−7760

(19) Ye, X.; Fei, J.; Diroll, B. T.; Paik, T.; Murray, C. B. Expanding the Spectral Tunability of Plasmonic Resonances in Doped Metal-Oxide Nanocrystals through Cooperative Cation−Anion Codoping. *J. Am. Chem. Soc.* **2014**, *136*, 11680−11686.
(20) Kanehara, M.; Koike, H.; Yoshinaga, T.; Teranishi, T. Indium Tin Oxide Nanoparticles with Compositionally Tunable Surface Plasmon Resonance Frequencies in the Near-IR Region. *J. Am. Chem. Soc.* **2009**, *131*, 17736−17737.
(21) Lounis, S. D.; Runnerstrom, E. L.; Bergerud, A.; Nordlund, D.; Milliron, D. J. Influence of Dopant Distribution on the Plasmonic Properties of Indium Tin Oxide Nanocrystals. *J. Am. Chem. Soc.* **2014**, *136*, 7110−7116.
(22) Tandon, B.; Yadav, A.; Khurana, D.; Reddy, P.; Santra, P. K.; Nag, A. Size-Induced Enhancement of Carrier Density, LSPR Quality Factor, and Carrier Mobility in Cr−Sn Doped In_2O_3 Nanocrystals. *Chem. Mater.* **2017**, *29*, 9360−9368.
(23) Hamberg, I.; Granqvist, C. G. Optical Properties of Transparent and Heat-Reflecting Indium Tin Oxide Films: The role of ionized impurity scattering. *Appl. Phys. Lett.* **1984**, *44*, 721−723.
(24) Hamberg, I.; Granqvist, C. G. Evaporated Sn-doped In_2O_3 films: Basic Optical Properties and Applications to Energy-Efficient Windows. *J. Appl. Phys.* **1986**, *60*, R123−R160.
(25) Zhang, D. H.; Ma, H. L. Scattering Mechanisms of Charge Carriers in Transparent Conducting Oxide Films. *Appl. Phys. A: Mater. Sci. Process.* **1996**, *62*, 487−492.
(26) Runnerstrom, E. L.; Bergerud, A.; Agrawal, A.; Johns, R. W.; Dahlman, C. J.; Singh, A.; Selbach, S. M.; Milliron, D. J. Defect Engineering in Plasmonic Metal Oxide Nanocrystals. *Nano Lett.* **2016**, *16*, 3390−3398.
(27) Mendelsberg, R. J.; Garcia, G.; Li, H.; Manna, L.; Milliron, D. J. Understanding the Plasmon Resonance in Ensembles of Degenerately Doped Semiconductor Nanocrystals. *J. Phys. Chem. C* **2012**, *116*, 12226−12231.
(28) Xu, J.; Liu, J. B.; Liu, B. X.; Li, S. N.; Wei, S. H.; Huang, B. Design of n-Type Transparent Conducting Oxides: The Case of Transition Metal Doping in In_2O_3. *Adv. Electron. Mater.* **2018**, *4*, 1700553.
(29) Bhachu, D. S.; Scanlon, D. O.; Sankar, G.; Veal, T. D.; Egdell, R. G.; Cibin, G.; Dent, A. J.; Knapp, C. E.; Carmalt, C. J.; Parkin, I. P. Origin of High Mobility in Molybdenum-Doped Indium Oxide. *Chem. Mater.* **2015**, *27*, 2788−2796.
(30) Tandon, B.; Shanker, G. S.; Nag, A. Multifunctional Sn- and Fe-Codoped In_2O_3 Colloidal Nanocrystals: Plasmonics and Magnetism. *J. Phys. Chem. Lett.* **2014**, *5*, 2306−2311.
(31) Tandon, B.; Yadav, A.; Nag, A. Delocalized Electrons Mediated Magnetic Coupling in Mn−Sn Codoped In_2O_3 Nanocrystals: Plasmonics Shows the Way. *Chem. Mater.* **2016**, *28*, 3620.
(32) Yadav, A.; Tandon, B.; Nag, A. Reduction of Mn^{3+} to Mn^{2+} and near infrared plasmonics from Mn-Sn codoped In_2O_3 nanocrystals. *RSC Adv.* **2016**, *6*, 79153−79159.
(33) Shanker, G. S.; Tandon, B.; Shibata, T.; Chattopadhyay, S.; Nag, A. Doping Controls Plasmonics, Electrical Conductivity, and Carrier-Mediated Magnetic Coupling in Fe and Sn Codoped In_2O_3 Nanocrystals: Local Structure Is the Key. *Chem. Mater.* **2015**, *27*, 892−900.
(34) Frank, G.; Köstlin, H. Electrical Properties and Defect Model of Tin-doped Indium Oxide Layers. *Appl. Phys. A: Solids Surf.* **1982**, *27*, 197−206.
(35) Warschkow, O.; Ellis, D. E.; González, G. B.; Mason, T. O. Defect Cluster Aggregation and Nonreducibility in Tin-Doped Indium Oxide. *J. Am. Ceram. Soc.* **2003**, *86*, 1707−1711.
(36) González, G. B.; Mason, T. O.; Quintana, J. P.; Warschkow, O.; Ellis, D. E.; Hwang, J.-H.; Hodges, J. P.; Jorgensen, J. D. Defect Structure Studies of Bulk and Nano-Indium-Tin Oxide. *J. Appl. Phys.* **2004**, *96*, 3912−3920.
(37) Staller, C. M.; Agrawal, A.; Gibbs, S. L.; Saez Cabezas, C. A.; Johns, R. W.; Milliron, D. J. Quantitative Analysis of Semiconductor Nanocrystal Ensemble Optical Extinction. *arXiv e-prints* **2018**. https://ui.adsabs.harvard.edu/abs/2018arXiv181210142S(accessed Dec 01, 2018).
(38) Zhang, Y. Electronegativities of Elements in Valence States and their Applications. 2. A Scale for Strengths of Lewis acids. *Inorg. Chem.* **1982**, *21*, 3889−3893.
(39) Zhang, Y. Electronegativities of Elements in Valence States and their Applications. 1. Electronegativities of Elements in Valence States. *Inorg. Chem.* **1982**, *21*, 3886−3889.
(40) Shannon, R. D.; Prewitt, C. T. Effective Ionic Radii in Oxides and Fluorides. *Acta Crystallogr., Sect. B: Struct. Crystallogr. Cryst. Chem.* **1969**, *25*, 925−946.
(41) Koida, T.; Kondo, M. High-Mobility Transparent Conductive Zr-doped In_2O_3. *Appl. Phys. Lett.* **2006**, *89*, 082104.
(42) Koida, T.; Kondo, M. Improved Near-Infrared Transparency in Sputtered In_2O_3-based Transparent Conductive Oxide Thin Films by Zr-doping. *J. Appl. Phys.* **2007**, *101*, 063705.
(43) Guilmeau, E.; Bérardan, D.; Simon, C.; Maignan, A.; Raveau, B.; Ovono, D. O.; Delorme, F. Tuning the Transport and Thermoelectric Properties of In_2O_3 Bulk Ceramics through Doping at In-site. *J. Appl. Phys.* **2009**, *106*, 053715.
(44) Jansons, A. W.; Hutchison, J. E. Continuous Growth of Metal Oxide Nanocrystals: Enhanced Control of Nanocrystal Size and Radial Dopant Distribution. *ACS Nano* **2016**, *10*, 6942−6951.
(45) Narayanaswamy, A.; Xu, H.; Pradhan, N.; Kim, M.; Peng, X. Formation of Nearly Monodisperse In_2O_3 Nanodots and Oriented-Attached Nanoflowers: Hydrolysis and Alcoholysis vs Pyrolysis. *J. Am. Chem. Soc.* **2006**, *128*, 10310−10319.
(46) Vegard, L. Die Konstitution der Mischkristalle und die Raumfüllung der Atome. *Eur. Phys. J. A* **1921**, *5*, 17−26.
(47) Nadaud, N.; Lequeux, N.; Nanot, M.; Jové, J.; Roisnel, T. Structural Studies of Tin-Doped Indium Oxide (ITO) and $In_4Sn_3O_{12}$[2]. *J. Solid State Chem.* **1998**, *135*, 140−148.
(48) Brewer, S. H.; Franzen, S. Calculation of the Electronic and Optical Properties of Indium Tin Oxide by Density Functional Theory. *Chem. Phys.* **2004**, *300*, 285−293.
(49) Jayakumar, O. D.; Gopalakrishnan, I. K.; Kulshreshtha, S. K.; Gupta, A.; Rao, K. V.; Louzguine-Luzgin, D. V.; Inoue, A.; Glans, P. A.; Guo, J. H.; Samanta, K.; Singh, M. K.; Katiyar, R. S. Structural and Magnetic Properties of $(In_{1-x}Fe_x)_2O_3$ ($0.0 \leqslant x \leqslant 0.25$) System: Prepared by Gel Combustion Method. *Appl. Phys. Lett.* **2007**, *91*, 052504.
(50) Farvid, S. S.; Hegde, M.; Radovanovic, P. V. Influence of the Host Lattice Electronic Structure on Dilute Magnetic Interactions in Polymorphic Cr(III)-Doped In_2O_3 Nanocrystals. *Chem. Mater.* **2013**, *25*, 233−244.
(51) Wagner, C. D.; Muilenberg, G. E. *Handbook of X-ray Photoelectron Spectroscopy: A Reference Book of Standard Data for Use in X-ray Photoelectron Spectroscopy*; Physical Electronics Division, Perkin-Elmer Corp.: Eden Prairie, MN, 1979.
(52) Dementjev, A. P.; Ivanova, O. P.; Vasilyev, L. A.; Naumkin, A. V.; Nemirovsky, D. M.; Shalaev, D. Y. Altered layer as Sensitive Initial Chemical State Indicator*. *J. Vac. Sci. Technol., A* **1994**, *12*, 423−427.
(53) Buonsanti, R.; Milliron, D. J. Chemistry of Doped Colloidal Nanocrystals. *Chem. Mater.* **2013**, *25*, 1305−1317.
(54) Crockett, B. M.; Jansons, A. W.; Koskela, K. M.; Johnson, D. W.; Hutchison, J. E. Radial Dopant Placement for Tuning Plasmonic Properties in Metal Oxide Nanocrystals. *ACS Nano* **2017**, *11*, 7719−7728.
(55) Erwin, S. C.; Zu, L.; Haftel, M. I.; Efros, A. L.; Kennedy, T. A.; Norris, D. J. Doping Semiconductor Nanocrystals. *Nature* **2005**, *436*, 91−94.

DOI: 10.1021/acs.chemmater.9b02917
Chem. Mater. 2019, 31, 7752−7760